

# Robust Unencapsulated Perovskite Solar Cells Protected by a Fluorinated Fullerene Electron Transporting Layer

Hsin-Hsiang Huang, Hsinhan Tsai, Rathinam Raja, Shu-Ling Lin, Dibyajyoti Ghosh, Cheng-Hung Hou, Jing-Jong Shyue, Sergei Tretiak, Wei Chen, King-Fu Lin, Wanyi Nie,\* and Leeyih Wang\*

Cite This: *ACS Energy Lett.* 2021, 6, 3376–3385

Read Online

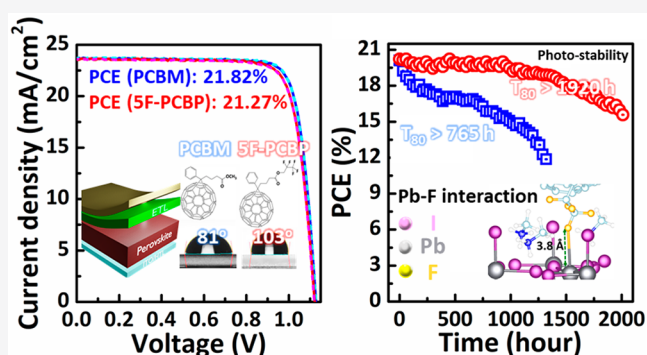
ACCESS |

Metrics & More

Article Recommendations

Supporting Information

**ABSTRACT:** The emergent perovskite photovoltaics technology faces challenges like the long-term durability combining moisture, thermal, and photo stresses that prevents them from competing with established technologies. Here, we introduce a series of new fluorinated fullerenes as an electron-transporting layer (ETL) for robust perovskite photovoltaics that deliver a high power conversion efficiency of 21.27% with substantially improved durability against environmental stressing. The hydrophobic nature of the new fullerene protects the unencapsulated perovskite cell with stability over 1400 h in 85% relative humidity. Notably, the unencapsulated device maintained 80% of their original performance ( $T_{80}$ ) after being immersed in water for over 10 min. Detailed characterizations suggest that the fluorinated fullerene can immobilize the cations in perovskites and passivate the surface traps. Therefore, the  $T_{80}$  lifetime of the devices under constant illumination reached 1920 h. On the basis of the accelerated test, we estimate a lifetime approaching 10 years with encapsulation. The successful demonstration of the new ETL can stimulate further research and momentum for future photovoltaic technology development.



Organic–inorganic halide perovskite photovoltaic technologies have demonstrated an unprecedented progress in less than a decade<sup>1</sup> with power conversion efficiency (PCE) of 25.5%, approaching the record of monocrystalline silicon devices.<sup>2</sup> Interests have arisen in the commercialization as well as the extension of the perovskite photovoltaic technologies for a new scope of green energy utilization and storage.<sup>3</sup> For example, the proposed concept of using perovskite solar cells (PSCs) to drive water splitting reactions for oxygen or hydrogen generation has opened up a new route toward efficient solar energy conversion into fuels that are easier for storage.<sup>4–6</sup> However, to fulfill the needs of the above-mentioned applications, the PSCs still lack the long-term operational stability under harsh environmental conditions.<sup>7</sup> Extensive studies have shown that moisture,<sup>8–12</sup> oxygen,<sup>13</sup> and high energy ultraviolet (UV) light<sup>14,15</sup> are the main factors governing the device lifetimes. External engineering controls can be employed, such as physical encapsulation<sup>16–18</sup> or UV filtration, to extend the devices' lifetimes. Whereas instability upon heat<sup>19–23</sup> and illumination<sup>24–28</sup> are inevitable for PSCs, even light-soaking can trigger device degradation<sup>29,30</sup> in an inert atmosphere. However, the

protections may not be always feasible for cases like solar-chemistry reactions where the cell has to make direct contact with water or aqueous media to donate/transfer electrons. It is therefore highly desirable to engineer the internal layers (i.e., electron or hole transporting layers) that can protect the cell from degradation while maintaining their electronic properties to deliver high power conversion efficiency.

Among various device architectures for thin-film PSCs, the inverted *p-i-n* structure that contains [6,6]-phenyl-C<sub>61</sub>-butyric acid methyl ester (PCBM) as the electron-transporting layer (ETL) is highly attractive because it shows a promising hysteresis-free current–voltage (*I*–*V*) characteristic,<sup>31–33</sup> efficient defect passivation,<sup>34</sup> and the ability to be processed under low temperature. However, the thin fullerene layer is not

Received: July 22, 2021

Accepted: August 26, 2021

Published: August 30, 2021



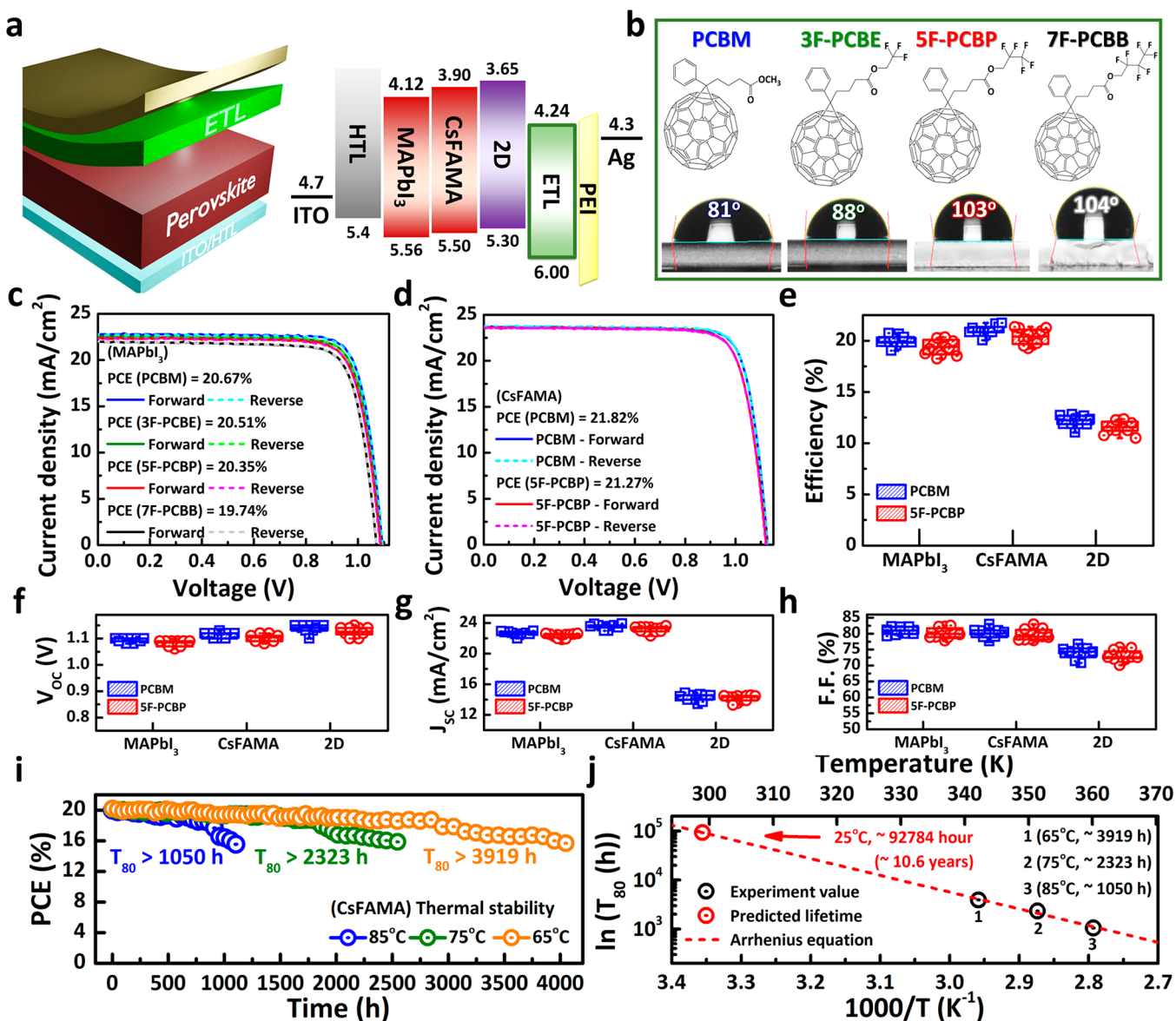


**Figure 1.** Device characterization. (a) Schematic illustration of the device architecture and associated energy band diagrams with each component. (b) The relative hydrophobicity of pristine PCBM and its new fluorinated derivatives. (c, d)  $J$ - $V$  characteristic curves for the champion MAPbI<sub>3</sub> and triple-cation (CsFAMA) perovskite devices that contain either 5F-PCBP (red) or PCBM (blue) as the ETL. (e–h) Statistics of PSCs for MAPbI<sub>3</sub> and CsFAMA as light absorbers with controls (PCBM) and fluorinated fullerene (5F-PCBP) over 12 different devices. (i) Normalized PCE of the CsFAMA device with 5F-PCBP vs storage time in the inert conditions at different temperatures. (j) Estimated device lifetime from Arrhenius fitting with  $T_{80}$  of the CsFAMA device with 5F-PCBP as a function of the reciprocal of the testing temperature.

sufficient to protect the perovskite active layer from moisture damage, and the fullerene molecules can undergo light-activated dimerization, thereby deteriorating the cell performance.<sup>35</sup> Promising strategies to tackle the stability issues have been reported;<sup>36,37</sup> for example, Chen et al. introduced an inorganic Ti(Nb)O<sub>x</sub> buffer layer on top of the PCBM that pushed the 3D perovskites device operational stability over 1000 h with external encapsulation.<sup>38</sup> Bai et al. developed a water-resistant cross-linkable silane-functionalized fullerene ETL in  $p$ - $i$ - $n$  PSCs, which helped to maintain almost 90% of the original PCE after one month of storage in an ambient environment, but the efficiency dropped rapidly to 70% of its initial value after 168 h under light-soaking in humid air.<sup>39</sup> Therefore, it is still essential to develop a novel material enhancing the humidity resistance and improving the thermal

and photo instability of perovskite devices without sacrificing photovoltaic performance. A well-known approach to effectively reduce the surface energy of an organic material is to incorporate fluorine atoms into the molecular structure. Such compounds are generally highly hydrophobic, which impart a repulsive property to water molecules. Bella et al. demonstrated a multifunctional fluoropolymer (Lumogen F Violet 570) to obtain considerably higher stability in PSCs without compromising the initial PCE.<sup>40</sup> Recently, fluorinated compounds as additives at the grain boundaries or surface of the perovskite have been widely used for passivating defects or suppressing halide anion vacancies as well as improving thermal and moisture stability, which should be a novel and effective approach for enhancing the device performance and long-term stability of PSCs.<sup>41,42</sup> Li et al. demonstrated that an

addition of NaF to the perovskites had a positive effect on passivating both the organic cation and halide anion vacancies, where the strong hydrogen bonding of N–H...F can immobilize organic cations (MA/FA) and consequently improves the thermal stability and photostability of the PSCs.<sup>42</sup>

Despite the initial promising demonstrations, an alternative efficient approach is to introduce a hydrophobic top contact layer while maintaining their transport properties.<sup>40</sup> Here, we synthesize a new series of ETL materials by strategically replacing the methyl-ester group in PCBM with a various number of fluoroalkyl segments (3F, 5F, and 7F) in the ester group in PCBM, which forms a compact layer and repulses water molecules from the PSCs by increasing surface hydrophobicity (see Note S1 and Figures S1 and S2). Our new ETL works well on the commonly used perovskites like triple-cation (CsFAMA) and methylamine lead triiodide (MAPbI<sub>3</sub>) as well as 2D perovskites and delivers a champion efficiency of 21.27% with excellent thermal and humidity resistance as well as photostability without the need for encapsulation. Specifically, MAPbI<sub>3</sub> devices maintain 80% of their original performance ( $T_{80}$ ) for >3000 h under a humid environment (relative humidity, RH = 50%) and >1000 h with thermal stability at 65 °C without a sign of degradation. Similarly, unencapsulated CsFAMA perovskites devices were evaluated under RH of 85% at room temperature and 85 °C in an inert atmosphere and maintained over 80% of the initial efficiency after >1440 and >1050 h of aging, respectively. We have further tested the devices by directly immersing them under water, and they maintained their performances at 90% for 120–300 s, whereas the pristine PCBM device degraded instantaneously. Surprisingly, the CsFAMA devices with 5F-PCBP sustained 70% PCE for >600 s. Detailed time-of-flight secondary ion mass spectroscopy reveals that the 5F-PCBP layer can immobilize the ions in the perovskite layer, which resolves the problem of mobile ion-induced instability under constant light. Supported by the coupled experimental characterizations and computational modeling, we found that the fluorinated fullerene increases the surface hydrophobicity, passivates the iodine vacancy, and immobilizes the organic ions on the perovskite surfaces. The most stable PSCs exhibit an PCE of ~21% along with extrapolated  $T_{80}$  lifetime of over 92 700 h when they are properly encapsulated, which would lead to shelf life testing approaching 10 years. Our study opens up a new vista for perovskite PV technologies to evolve toward commercialization as well as to a broad range of green energy applications.

We first synthesized a series of fullerene derivatives (3F-PCBE, 5F-PCBP, and 7F-PCBB) with different lengths of fluorocarbon chains to improve the hydrophobicity in comparison to the conventional PCBM ETL (the structures are shown in Figure 1a,b). The processing solvents were engineered to optimize the crystalline packing in the fullerene layer to achieve an ideal contact angle and surface morphology (see Note S2, Figures S3 and S4, and Table S1). Note that the crystalline packing of the ETL enhances the surface hydrophobicity of the fluorinated-ETL (F-ETL) by solvent engineering. We first probe the surface energies of the F-ETLs by the contact angle method using deionized water; the results are shown in Figure 1b. The contact angle for the pristine PCBM surface is 81°, and as the number of fluorines incorporated into the PCBM increases, this angle increases to up to 104°, suggesting improved hydrophobicity.

To investigate the photovoltaic device performance using the modified fullerenes, we further fabricated a *p-i-n* device in the architecture of indium tin oxide (ITO)/hole transporting layer (HTL)/perovskite layer/fullerene/polyethylenimine/Ag (Figure 1a). Here, we use poly[3-(6-carboxyhexyl) thiophene-2,5-diyl] (P3HT-COOH) as the HTL<sup>43</sup> and classical methylammonium lead triiodide (MAPbI<sub>3</sub>) and commonly studied triple-cation perovskites (Cs<sub>0.05</sub>FA<sub>0.78</sub>MA<sub>0.17</sub>PbI<sub>2.53</sub>Br<sub>0.47</sub>, CsFAMA) as the light absorber (see the basic characterizations of the perovskite layer in Note S3 and Figures S5 and S6). From the current density–voltage (*J*–*V*) curves, the efficiency decreases with an increase in the number of fluorine atoms. After considering the surface energy (Figure 1b) and layer coverage (Figure S3), we decided to proceed with 5F-PCBP as the ETL for detailed performance testing. According to the cross-sectional scanning emission microscopy (SEM) image in Figure S7, the thickness for the ETL is 70 nm. The *J*–*V* characteristic curves obtained from the *p-i-n* photovoltaic devices under simulated AM1.5G white light illumination with 1-sun equivalent intensity are plotted in Figure 1c,d. The devices with PCBM and 5F-PCBP ETLs have comparable performances for both the MAPbI<sub>3</sub> device (PCBM: 20.67%; 5F-PCBP: 20.35%) and the CsFAMA device (PCBM: 21.82%; 5F-PCBP: 21.27%), as shown in Figure 1e–h, while Table S2 summarizes the corresponding figure-of-merit parameters (see details in Note S4 and Figures S8–S10). The external quantum efficiency (EQE) for the CsFAMA device is shown in Figure S11. Furthermore, the hysteresis effects are negligible in both cases when scanning the voltage in different polarities (Figures 1c,d and S12). We also extend the study using our 5F-PCBP ETL on two-dimensional (2D) Ruddlesden–Popper PSCs (PEA<sub>2</sub>MA<sub>4</sub>Pb<sub>3</sub>I<sub>16</sub>) (Figures 1e–h and S13 and Table S1) that show 12.05% efficiency. These results suggest that 5F-PCBP maintains the favorable energy band alignment similar to PCBM, which generally applies to single junction perovskites cells and tandem devices without sacrificing the performance. The energy alignments for PCBM and 5F-PCBP were further determined by photoelectron spectroscopy in the air (Figures 1a and S14) and supported by computational simulations (Figure S15). Interestingly, the incorporation of fluorine atoms in 5F-PCBP does not have a huge impact on the energy level, as shown in Figure S15, because both the highest occupied molecular orbital (HOMO) and lowest unoccupied molecular orbital (LUMO) of PCBM and 5F-PCBP are delocalized over the C<sub>60</sub> moiety, as revealed by the charge density plots. In addition, the electron mobilities of PCBM and 5F-PCBP were obtained from the space-charge limited current (SCLC) measurement resulting in  $4.19 \pm 0.51 \times 10^{-4}$  and  $2.27 \pm 0.75 \times 10^{-4}$  cm<sup>2</sup> V<sup>-1</sup> s<sup>-1</sup> values, respectively (Figure S16). The electron mobility of PCBM is comparable to the reported value,<sup>44</sup> while that for 5F-PCBP is slightly lower, and can likely be further improved by optimizing the molecular packing.

In order to assess the operational stability of the device fabricated with PCBM and 5F-PCBP as the ETL, we designed a series of environmental stressing conditions to age the device without additional encapsulations. This includes heat stress (65–85 °C), moisture exposure (RH = 50–85%), water immersion, and constant illumination (100 mW/cm<sup>2</sup>). We test each condition separately in order to understand the degradation mechanisms; all data were collected over 20 devices in several batches for statistics. First of all, many studies have suggested that perovskites containing methylamine are

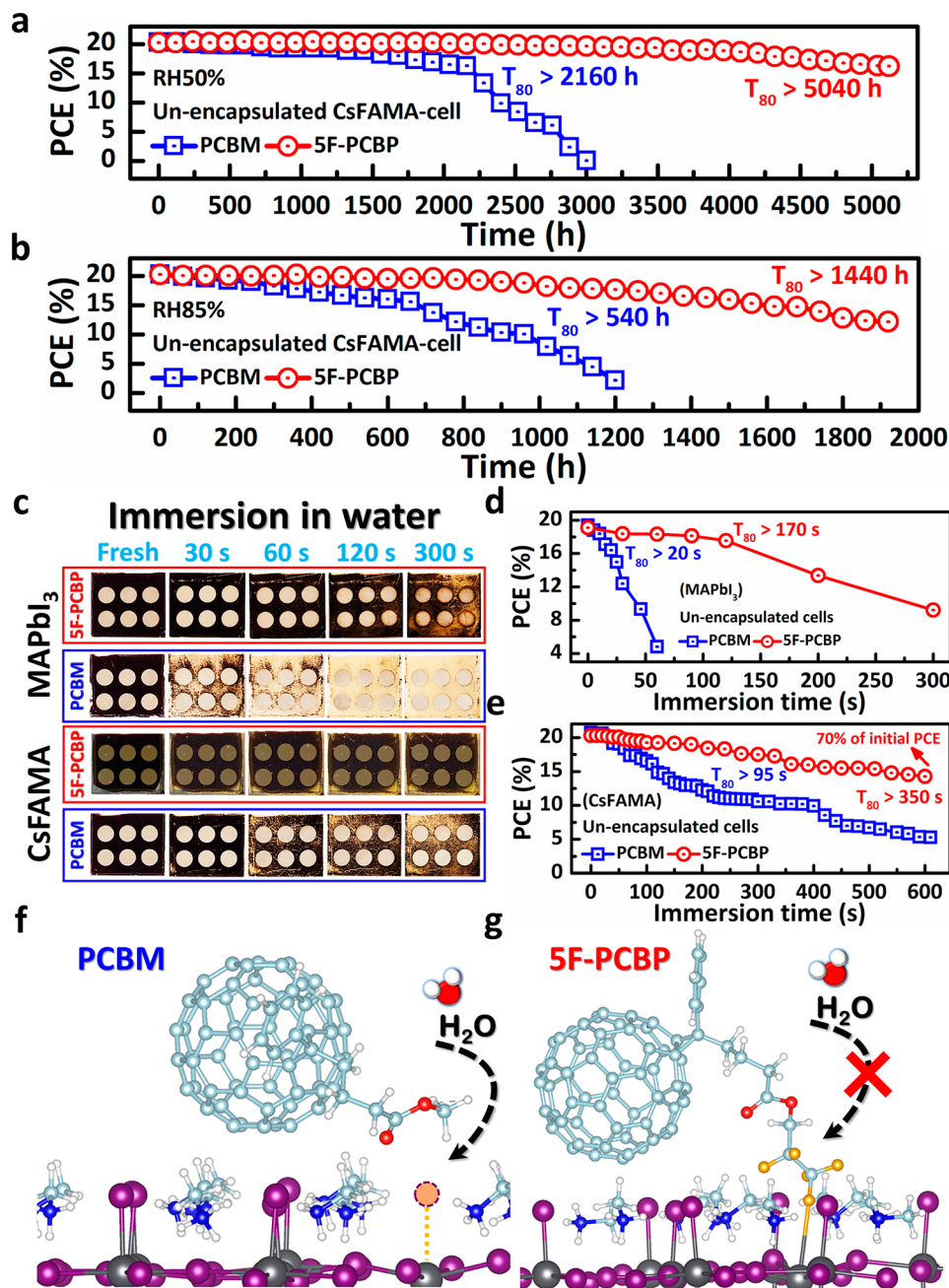


**Figure 2.** Moisture testing. The normalized PCE as a function of (a) 50% and (b) 85% humidity exposure time. (c) The photos of the full MAPbI<sub>3</sub> and CsFAMA PSCs taken after various immersion times in water for 5F-PCBP (top) and PCBM (bottom) devices. Normalized PCE of (d) MAPbI<sub>3</sub> and (e) CsFAMA devices as a function of water immersion time. The optimized structure of the (f) perovskite/PCBM and (g) perovskite/5F-PCBP interface with the iodine vacancy on the surface of the perovskite. Key colors: hydrogen (white), carbon (pale cyan), oxygen (red), nitrogen (blue), iodine (purple), and lead (dark gray). The approximate iodine vacancy site has been marked with a pale orange sphere.

thermally unstable even in an inert environment<sup>45</sup> and can back convert into PbI<sub>2</sub> and release CH<sub>3</sub>I or NH<sub>3</sub> gases.<sup>46</sup> However, the solar modules should also sustain a high temperature while generating energy. Therefore, we first investigate the 5F-PCBP and PCBM devices under constant heat stress in an inert atmosphere; the results are plotted in Figures 1i,j and S17. Figure 1i shows the industrial standard thermal stability test (85 °C) for the CsFAMA perovskites devices in nitrogen. The CsFAMA/5F-PCBP device shows a prolonged  $T_{80}$  of 1050 h, two times longer than that of the CsFAMA/PCBM device ( $T_{80} = 432$  h as shown in Figure

S17b). To understand the mechanism of the thermal instability, the photovoltaic device parameters of the PCBM and 5F-PCBP cells were extracted (Figure S18). Interestingly, the rapid performance decay in the first 300 h (MAPbI<sub>3</sub> device) and 576 h (CsFAMA device) of the PCBM cell mainly comes from the decrease of  $V_{OC}$ , whereas its  $J_{SC}$  remains unchanged. The decay of fill factor (FF) in the PCBM cell is associated with the decrease in shunt resistance ( $R_{sh}$ ) (see  $J-V$  curves in Figure S18a). We use atomic force microscopy (AFM) and the cross-sectional SEM images (Figures S19–S20) to investigate the morphology change

after thermal stress. From the AFM images (Figure S19), both PCBM and SF-PCBP layers in the freshly-prepared devices are smooth and uniform with a roughness of 1.59 and 1.76 nm, respectively. After heat treatment at 65 °C for 600 h, the SF-PCBP layer remains uniform and the roughness slightly increases to 1.93 nm, which indicates the absence of substantial changes in the subnanometer scale (Figure S19a, bottom right). However, we observed a serious layer deformation in the annealed PCBM layer (Figure S19a, bottom left, and Figure S20) with much higher surface roughness (4.96 nm) than freshly-prepared PCBM film (1.59 nm). This is mainly attributed to the PCBM molecule aggregation into crystalline clusters upon the high-temperature treatment (Figures S20 and S21) as also observed in previous reports.<sup>37,47</sup> These results suggest that the relative bulky pentafluoropropyl ester group may act as an aggregation inhibitor to suppress the thermal coagulation in SF-PCBP through the  $\pi$ - $\pi$  interaction between C<sub>60</sub> cages, largely improving the morphological stability under a high temperature (see Note S5 and Figure S22). Therefore, the PCBM aggregation-induced roughness change further increases the carrier recombination and consequently deteriorates the  $R_{sh}$  and  $V_{OC}$  in the  $J$ - $V$  curves (Figure S23). Furthermore, the deformation layer of PCBM also expedites the AgI formation, which will alter the work function and reduce the charge-carrier collection efficiency of the electrode (see Note S6 and Figures S24 and S25).

In addition, one of the most popular methodologies to extrapolate the organic solar device lifetime is based on the Arrhenius relationship,<sup>48,49</sup> which assumes that a material degradation process is controlled by a degradation rate ( $k_d$ ) and proportional to  $\exp(-E_a/k_B T)$ , where  $E_a$  is the activation energy of a failure condition and  $k_B$  and  $T$  are the Boltzmann constant and the temperature in Kelvin, respectively. Accordingly, we employ the Arrhenius equation to estimate the storage lifetime of the CsFAMA/SF-PCBP device at inert conditions. The normalized PCEs of the PSCs with SF-PCBP versus storage time in the glovebox at 65, 75, and 85 °C are plotted in Figure 1i. The  $T_{80}$  lifetimes of the PSCs with SF-PCBP at 65, 75, and 85 °C were estimated to be 3919, 2323, and 1050 h, respectively. This result suggests that, by the calculation, the lifetime (shelf life test) of the PSCs with SF-PCBP at room temperature (298 K) can be estimated to be over 92 700 h, or approximately over 10 years, as shown in Figure 1j. These impressive results unveil that using the SF-PCBP ETL can largely improve device long-term thermal stability to a practical level.

Apart from the impact of the thermal stability, we stress the cells under moisture exposure and water immersion; the device performances are summarized in Figure 2. We first characterize the devices being stored in an ambient environment with RH of 50% and 85% (Figures 2a,b and S26), and the  $J$ - $V$  curves are shown in Figure S27a. Under RH = 50%, the PCE for the unencapsulated CsFAMA/SF-PCBP device in Figure 2a exhibits a substantially improved stability with  $T_{80}$  = 5040 h. In sharp contrast, the normalized PCE for the unencapsulated CsFAMA/PCBM device undergoes rapid degradation of  $T_{80}$  in 2160 h and losses its function within 3000 h. We further evaluated the unencapsulated CsFAMA/SF-PCBP device in industrial standard humidity conditions (RH = 85%); the cell  $T_{80}$  is 1440 h (Figure 2b). In striking contrast again, the CsFAMA/PCBM devices quickly decrease to 80% of their initial PCE after 540 h. When taking a closer look at the evolution of photovoltaic parameters for the PCBM device in

Figure S27b, the  $J_{SC}$  drops concomitant to an increase in series resistance ( $R_s$ ), while its  $V_{OC}$  is maintained relatively longer. The fast decrease in  $J_{SC}$  and increase in  $R_s$  suggest that high humidity has converted part of the perovskite material back into the insulating PbI<sub>2</sub> precursor phase<sup>48</sup> that mitigates the charge collection. On the other hand, the moisture resistance nature of SF-PCBP (Figure 1b) can protect the photoactive layer much better over time. To testify the photovoltaic performance of the PSCs under much harsher moisture conditions, we immersed the unencapsulated PCBM and SF-PCBP devices into a deionized water bath at room temperature and tested the device performance as a function of immersion durations. The images and normalized PCE of the devices obtained from SF-PCBP and PCBM as a function of the immersion time period are shown in Figure 2c-e. For the device with SF-PCBP after 300 s under water, the CsFAMA device showed no sign of degradation, whereas the MAPbI<sub>3</sub> device had a slight decomposition (Figure 2c, MAPbI<sub>3</sub>-top). However, the MAPbI<sub>3</sub>/PCBM device (Figure 2c, MAPbI<sub>3</sub> bottom) starts the degradation immediately after immersion and completely turns into palm yellow after 30 s. In addition, the CsFAMA/PCBM device maintains most of its color in water in the same period (Figure 2c, CsFAMA bottom) and initiates the degradation process after 60 s. From the time evolution as a function of the device PCE plot in Figure 2d, we find that the MAPbI<sub>3</sub>/SF-PCBP device performance retains over 90% of its initial performance after 120 s of immersion and shows an impressive  $T_{80}$  = 170 s. On the contrary, the MAPbI<sub>3</sub>/PCBM device degrades immediately with  $T_{80}$  of 20 s and becomes nonfunctional in less than 60 s of immersion (Figure 2d). More impressively, the CsFAMA/SF-PCBP device (Figure 2e) shows an encouraging lifetime over 600 s, maintaining over 70% of its initial peak PCE. The CsFAMA/PCBM device completely degraded with  $T_{80}$  of 95 s. In addition, we have also tested the 2D (PEA<sub>2</sub>MA<sub>4</sub>Pb<sub>3</sub>I<sub>16</sub>) perovskite device stability with the protection of the SF-PCBP layer under water; the 2D devices maintained 80% of their initial PCE after 510 s, which is three times longer than the PCBM device ( $T_{80}$  = 140 s) shown in Figure S28. These demonstrations suggest that SF-PCBP ETL can be widely applicable to protect all popular perovskite absorbing layers. Multiple characterizations including X-ray diffraction (XRD), ultraviolet-visible (UV-vis) spectroscopy, and EQE data (see Notes S7 and S8 and Figures S29-S36) exhibited good agreement with our finding; i.e., the incorporation of F atoms onto the fullerene-based ETL can effectively protect the cell from moisture degradation.

To gain deeper insight into the protection mechanism from SF-PCBP, we computationally model to the perovskites/ETL interfaces and simulate possible interactions between the perovskite defect surface and the C<sub>60</sub>-based molecules (Figure 2f,g). From the simulation results, the PCBM molecule mostly retains its geometry as found on the pristine perovskite surface (Figure 2f, Notes S9 and S10 and Figures S37-S40). In the case of the SF-PCBP molecules, on the other hand, we found that, along with the fact that it increases the hydrophobicity, it also acts as a partial defect passivating agent. Optimized geometry exhibits that the end F atom of the fluorinated butyric acid group orients toward the surface and that in turn passivates the iodine vacancy sites (Figures 2g and S40) commonly present on the MAPbI<sub>3</sub> surface. The iodide vacancy induced surface defects are commonly observed in hybrid perovskites due to their low formation energies.<sup>50</sup> Although the

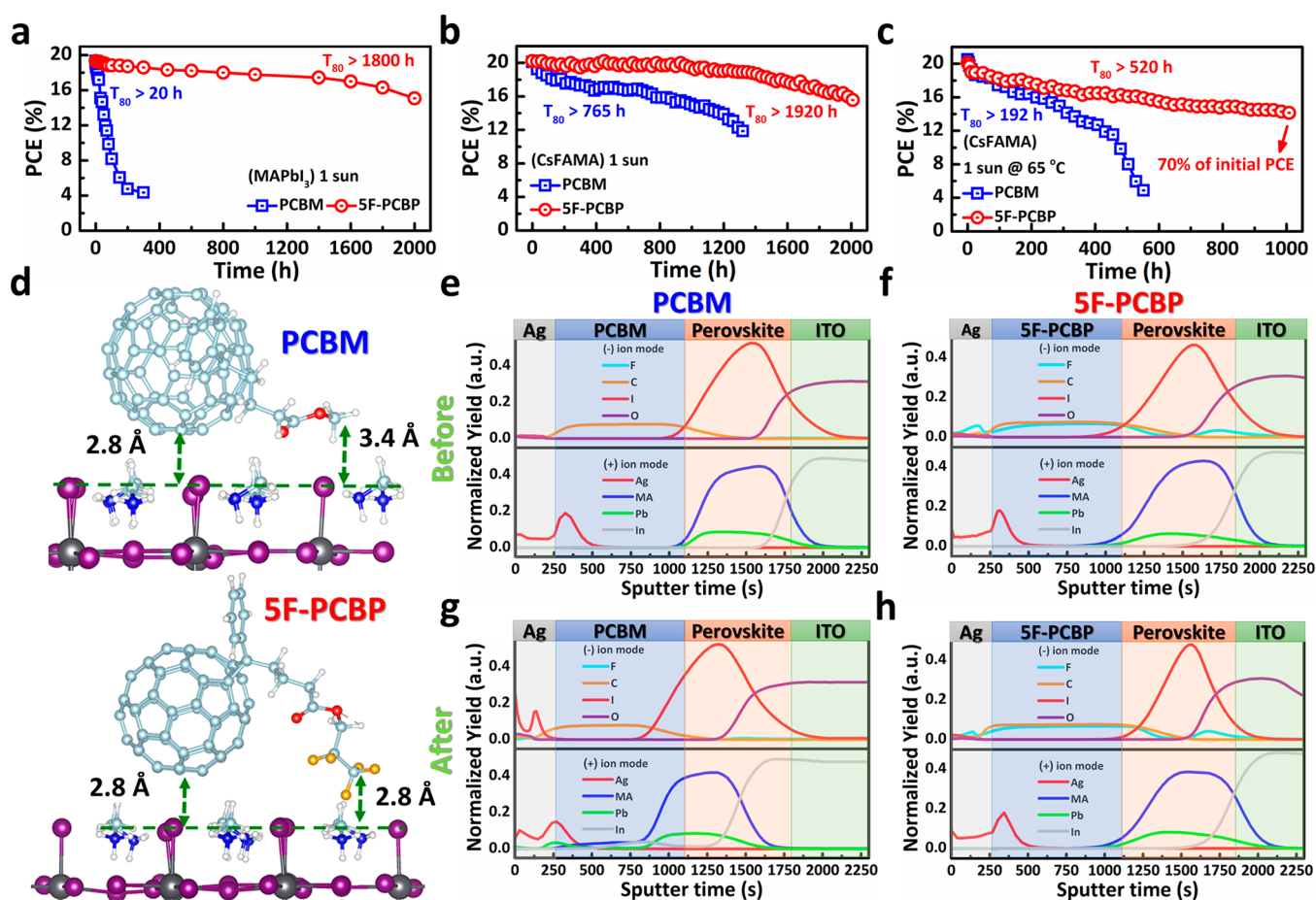


**Figure 3.** Photoinduced ion migration and degradation mechanism. Photostability test of (a) MAPbI<sub>3</sub> and (b) CsFAMA devices under constant 1 sun illumination with a full-spectrum AM1.5G source. (c) Photostability performance of the unencapsulated CsFAMA devices under full-spectrum sunlight at 65 °C. (d) Optimized geometries of the perovskite surface with PCBM and SF-PCBP molecules. In both structures, the C<sub>60</sub> ring is on the top of the surface iodine atoms. ToF-SIMS depth profile across the whole device for freshly-prepared devices and degraded devices after 200 h of constant AM1.5G 1 sun illumination in a nitrogen atmosphere with PCBM (e and g) and SF-PCBP (f and h).

perovskites have high tolerance to those defects in the electronic properties, the iodine vacancy can play a central role in initiating degradation in halide perovskites in the presence of water.<sup>51–53</sup> Mosconi et al. have shown that the iodine vacancy on the surface forms undercoordinated Pb atoms, which get dissolved in water at a much faster rate compared to that for defect-free surfaces.<sup>51</sup> Thus, the iodine vacancy passivation has been one of the promising approaches to enhance the halide perovskites stability under humidity.

Finally, the photostability of the unencapsulated devices is investigated under constant 1 sun illumination with an AM1.5G filter in an inert atmosphere. Figure 3a compares the performance degradation curves of the MAPbI<sub>3</sub> devices with these two ETLs. Under constant light stress, the MAPbI<sub>3</sub>/SF-PCBP devices are more stable with an impressive T<sub>80</sub> lifetime of over 1800 h. In contrast, the MAPbI<sub>3</sub>/PCBM device has a short T<sub>80</sub> lifetime of lower than 20 h. We further correlate the corresponding photovoltaic parameters with the light irradiation time (Figure S41a). The MAPbI<sub>3</sub>/SF-PCBP devices V<sub>OC</sub>, J<sub>SC</sub>, and FF are stable for over 1500 h with a slight drop after 2000 h of constant illumination. For the MAPbI<sub>3</sub>/PCBM cell, however, the performance decay is mainly attributed to the fast drop in FF at the initial stage, leading to a rapid deterioration of device performance. Moreover, we

also test the photostability of the CsFAMA devices; as shown in Figure 3b, the CsFAMA/SF-PCBP device shows a T<sub>80</sub> lifetime exceeding 1920 h, which is much longer than that of the CsFAMA/PCBM device (765 h). In order to more intuitively reflect the advancement of our strategy (fluorinated fullerene) in stability design, the comparison of photostability from the previous results has been conducted as shown in Figure S42 (see the details in Note S11). We also performed an accelerated test by monitoring the PCE under various light intensities (1 to 5 sun illumination), as shown in Figure S43 (see the details in Note S12). It is explicit to see that our simply modified ETL (SF-PCBP) sustains the device photostability as well as those nontrivial instability-mitigation approaches. Having demonstrated the improved photostability of the SF-PCBP device, we proceed to investigate the stability of the complete photovoltaic cells under combined heat and light stresses. We then test the stability of the unencapsulated devices under full-spectrum sunlight at 65 °C and show the evolution of the device performance in Figure 3c. We find a very slow degradation of the PSCs based on the SF-PCBP ETL device, which retains about 70% of their initial performance after 1000 h of aging. In contrast, the control device quickly decreases to T<sub>80</sub> after roughly 190 h and then degrades swiftly to nil within ~550 h. A further study is indeed needed to

understand the degradation mechanism of the combined environmental conditions.

We attribute the observed improvement in the photostability to two origins: (1) steric hindrance in 5F-PCBP preventing dimerization upon light exposure, which is commonly observed in PCBM;<sup>54,55</sup> (2) immobilized ions at the perovskite surface by 5F-PCBP. To probe the first effect, the photo triggered dimerization process of the PCBM and 5F-PCBP layers is first examined using a UV–vis absorption (Figure S44), where the gradual formation of dimers in the PCBM layer under constant light irradiation corresponds to a concomitant increase of absorbance at 320 nm.<sup>56</sup> On the other hand, the decreasing FF can also be attributed to the second effect, where the mobile ion can corrode the Ag top electrode that forms AgI defects at the interface, surfaces, and grain boundaries,<sup>57,58</sup> consistent with the observed trap-state density results (see Note S13 and Figures S45 and S46). To provide an atomistic model for the ion immobilization process by the F-ETL, we employ quantum chemical calculations to construct the interface, particularly focusing on the organic cations. Our simulation results show that, apart from filling the iodine vacancy shown in Figure 2f,g, the fluorine in 5F-PCBP near the perovskite surface can also form a hydrogen bond (H-bond) with the surrounding MA cations (Figure 3d) by facilitating different types of energetically stable local conformations. Such a noncovalent bond formation with the perovskite surface further justifies the favorable perpendicular orientation of the butyrate chain of the 5F-PCBP molecules. These intermolecular forces between 5F-PCBP and the MA<sup>+</sup> cation on the perovskites/5F-PCBP interface stabilize the exposed MAI surface and further suppress the ion migration from the surface to the 5F-PCBP/Ag interface (see Note S14 and Figures S47 and S48). Moreover, the strong H-bond formation between 5F-PCBP and the surface MA<sup>+</sup> cations further explains the better stability in perovskite/5F-PCBP interfaces compared to perovskite/PCBM interfaces under heat stress (see Note S15 and Figure S49). The evaporation of surface MA<sup>+</sup> molecules has been attributed to the surface degradation induced by thermal stress in perovskites.<sup>59,60</sup> The H-bonds between 5F-PCBP and MA certainly stabilize the surface of the perovskite and hinder the escape of the organic cations (Figures 3d and S48).

Photoinduced ion migration in perovskite photovoltaics has recently attracted enormous attention<sup>61,62</sup> because it significantly affects the device reproducibility and stability. As such, we carefully examine the longitudinal distribution of elements in devices using time-of-flight secondary ion mass spectroscopy (ToF-SIMS), which exclusively probes the effect of ion migrations. Figure 3e–h shows the ToF-SIMS depth profiles of the entire device using PCBM and 5F-PCBP as the ETL before and after 200 h of constant illumination. Here, each layer component across the cathode (Ag) to the anode (ITO) is labeled according to the intensity of ion counts. Compared to the fresh device, the early appearing interface positions and the migrated component signals (e.g., I in the Ag region, MA and Pb in the PCBM region) indicate a reduced thickness and a less well-defined layered structure of the degraded PCBM device after the 200 h constant illumination (Figure 3g). On the other hand, the 5F-PCBP device completely hinders the component migration (Figure 3h), which is beneficial to material and device operation stability. These results indicate two important facts: (1) Upon photoexcitation, the Pb–I bonds are subject to distortion and volatile organic cations may escape out of the crystal lattice, resulting in the decomposition

of the perovskite crystals. (2) The Pb–I bond breaking on the surface of the perovskite by light creates cation and anion vacancies that facilitate the release of I<sup>−</sup> and MA<sup>+</sup> from the perovskite<sup>63</sup> and the ion migration.

In summary, we demonstrate novel fluorinated fullerene-based ETLs to enhance the materials and device stability without sacrificing the performance. By detailed device characterizations and theoretical modeling, we probed the key factors governing the device operational stability, which elucidated the origin of the degradation. These novel fluorinated fullerene-based ETLs not only act as hydrophobic protection layers but also can passivate the vacancy on the interface, which prohibits the water molecule penetration as well as the ion migration in the perovskite materials. As a result, the unencapsulated 5F-PCBP devices exhibit a remarkable photovoltaic operation lifetime under continuous humidity conditions, heat stress, and illumination environments. Importantly, we demonstrated the greatly improved cell stability under water, showing that the PSCs could potentially be used in water and other aqueous media to facilitate the solar driven electrical chemical reactions. These demonstrations also showed that the perovskite photovoltaic technologies have the potential to be commercialized and used in a broad range of green energy and storage applications.

## ■ ASSOCIATED CONTENT

### Supporting Information

The Supporting Information is available free of charge at <https://pubs.acs.org/doi/10.1021/acseenergylett.1c01526>.

Detail experimental conditions, material characterizations, additional discussion, surface morphology and contact angles, optical spectra, X-ray diffraction patterns, SEM and AFM images, XPS and EDX analysis, <sup>1</sup>H NMR data, FTIR, <sup>19</sup>F NMR, TGA, UV–vis, and steady state PL and TRPL spectra, EIS measurements, *J–V* curves, EQE spectra, PESA analysis, computational simulations data, device stability test, PCE analysis, photovoltaic parameters, computationally optimized structures, bond lengths, charge extraction property analysis, table of surface energy, and table of photovoltaics parameters (PDF)

Video demonstrated the perovskites thin films immersion test in water with PCBM and 5F-PCBP as ETL (MP4)

## ■ AUTHOR INFORMATION

### Corresponding Authors

Leeyih Wang – Centre for Condensed Matter Sciences, National Taiwan University, Taipei 10617, Taiwan; Center of Atomic Initiative for New Materials and Institute of Polymer Science and Engineering, National Taiwan University, Taipei 10617, Taiwan; [orcid.org/0000-0002-6368-0141](https://orcid.org/0000-0002-6368-0141); Email: [leewang@ntu.edu.tw](mailto:leewang@ntu.edu.tw)

Wanyi Nie – Center for Integrated Nanotechnologies, Los Alamos National Laboratory, Los Alamos, New Mexico 87545, United States; [orcid.org/0000-0002-5909-3155](https://orcid.org/0000-0002-5909-3155); Email: [wanyi@lanl.gov](mailto:wanyi@lanl.gov)

### Authors

Hsin-Hsiang Huang – Centre for Condensed Matter Sciences, National Taiwan University, Taipei 10617, Taiwan; Department of Materials Science and Engineering, National

Taiwan University, Taipei 10617, Taiwan; Materials Science Division and Center for Molecular Engineering, Argonne National Laboratory, Lemont, Illinois 60439, United States

**Hsinhan Tsai** – Center for Integrated Nanotechnologies, Los Alamos National Laboratory, Los Alamos, New Mexico 87545, United States

**Rathinam Raja** – Centre for Condensed Matter Sciences, National Taiwan University, Taipei 10617, Taiwan

**Shu-Ling Lin** – Centre for Condensed Matter Sciences, National Taiwan University, Taipei 10617, Taiwan; Institute of Organic and Polymeric Materials, National Taipei University of Technology, Taipei 10608, Taiwan

**Dibyajyoti Ghosh** – Physics and Chemistry of Materials and Center for Nonlinear Studies, Los Alamos National Laboratory, Los Alamos, New Mexico 87545, United States; Present Address: Department of Materials Science and Engineering and Department of Chemistry, Indian Institute of Technology, Delhi, Hauz Khas, New Delhi 110016, India; [orcid.org/0000-0002-3640-7537](https://orcid.org/0000-0002-3640-7537)

**Cheng-Hung Hou** – Research Center for Applied Science, Academia Sinica, Taipei 11529, Taiwan; [orcid.org/0000-0002-5150-7106](https://orcid.org/0000-0002-5150-7106)

**Jing-Jong Shyue** – Research Center for Applied Science, Academia Sinica, Taipei 11529, Taiwan; [orcid.org/0000-0002-8508-659X](https://orcid.org/0000-0002-8508-659X)

**Sergei Tretiak** – Center for Integrated Nanotechnologies, Los Alamos National Laboratory, Los Alamos, New Mexico 87545, United States; Physics and Chemistry of Materials and Center for Nonlinear Studies, Los Alamos National Laboratory, Los Alamos, New Mexico 87545, United States; [orcid.org/0000-0001-5547-3647](https://orcid.org/0000-0001-5547-3647)

**Wei Chen** – Materials Science Division and Center for Molecular Engineering, Argonne National Laboratory, Lemont, Illinois 60439, United States; Pritzker School of Molecular Engineering, University of Chicago, Chicago, Illinois 60637, United States; [orcid.org/0000-0001-8906-4278](https://orcid.org/0000-0001-8906-4278)

**King-Fu Lin** – Department of Materials Science and Engineering, National Taiwan University, Taipei 10617, Taiwan; [orcid.org/0000-0002-4187-9424](https://orcid.org/0000-0002-4187-9424)

Complete contact information is available at:

<https://pubs.acs.org/10.1021/acsenergylett.1c01526>

### Author Contributions

L.W. and K.-F.L. conceived this study and planned the experiments. H.-H.H. fabricated all the devices and performed all the measurements. R.R. synthesized a series of fluorinated ETL. S.-L.L. helped with stability data collection. C.-H.H. and J.-J.S. helped carry out the ToF-SIMS experiment and data analysis. D.G. and S.T. performed DFT-based computational modeling. W.C. helped with data analysis. H.T. and W.N. analyzed the data and provided insight into writing the paper. L.W., K.-F.L., H.-H.H., H.T., and W.N. jointly wrote the manuscript. All authors discussed the results and contributed to the final manuscript.

### Notes

The authors declare no competing financial interest.

### ACKNOWLEDGMENTS

This work was financially supported by the Ministry of Science and Technology, Taiwan (MOST 108-2113-M-002-015-MY3; 108-2911-I-002-561), Academia Sinica, Taiwan (AS-iMATE-

109-31) and the Center of Atomic Initiative for New Materials, National Taiwan University from the Featured Areas Research Center Program within the framework of the Higher Education Sprout Project by the Ministry of Education, Taiwan. H.-H.H. acknowledges the financial support from Ministry of Science and Technology, Taiwan (MOST 108-2911-I-002-561). This work was performed, in part, at the Center for Integrated Nanotechnologies, an Office of Science User Facility operated for the U.S. Department of Energy (DOE) Office of Science and the Center for Nonlinear Studies (CNLS) at Los Alamos National Laboratory (LANL). Work performed by W.N. is supported by the LANL-LDRD program (20180026DR). H.T. acknowledges the financial support from J. Robert Oppenheimer (JRO) Distinguished Postdoc Fellowship at LANL.

### REFERENCES

- (1) *Best Research-Cell Efficiency Chart*; <https://www.nrel.gov/pv/assets/pdfs/best-research-cell-efficiencies.20200406.pdf> (accessed April 2020).
- (2) Wang, P.; Li, G.; Wang, M.; Li, H.; Zheng, J.; Yang, L.; Chen, Y.; Li, D.; Lu, L. Numerical study of mono-crystalline silicon solar cells with passivated emitter and rear contact configuration for the efficiency beyond 24% based on mass production technology. *J. Semicond.* **2020**, *41* (6), 062701.
- (3) Balzani, V.; Pacchioni, G.; Prato, M.; Zecchina, A. Solar-driven chemistry: towards new catalytic solutions for a sustainable world. *Rend. Lincei Sci. Fis. Nat.* **2019**, *30* (3), 443–452.
- (4) Huang, Y.; Liu, J.; Deng, Y.; Qian, Y.; Jia, X.; Ma, M.; Yang, C.; Liu, K.; Wang, Z.; Qu, S.; Wang, Z. The application of perovskite materials in solar water splitting. *J. Semicond.* **2020**, *41* (1), 011701.
- (5) Zhang, H.; Lu, Y.; Han, W.; Zhu, J.; Zhang, Y.; Huang, W. Solar energy conversion and utilization: Towards the emerging photoelectrochemical devices based on perovskite photovoltaics. *Chem. Eng. J.* **2020**, *393*, 124766.
- (6) Singh, S.; Chen, H. J.; Shahrokhi, S.; Wang, L. P.; Lin, C. H.; Hu, L.; Guan, X. W.; Tricoli, A.; Xu, Z. J.; Wu, O. Hybrid Organic-Inorganic Materials and Composites for Photoelectrochemical Water Splitting. *ACS Energy Lett.* **2020**, *5* (5), 1487–1497.
- (7) Khenkin, M. V.; Katz, E. A.; Abate, A.; Bardizza, G.; Berry, J. J.; Brabec, C.; Brunetti, F.; Bulović, V.; Burlingame, Q.; Di Carlo, A.; Cheacharoen, R.; Cheng, Y.-B.; Colsmann, A.; Cros, S.; Domanski, K.; Duszka, M.; Fell, C. J.; Forrest, S. R.; Galagan, Y.; Di Girolamo, D.; Grätzel, M.; Hagfeldt, A.; von Hauff, E.; Hoppe, H.; Kettle, J.; Köbler, H.; Leite, M. S.; Liu, S.; Loo, Y.-L.; Luther, J. M.; Ma, C.-Q.; Madsen, M.; Manceau, M.; Matheron, M.; McGehee, M.; Meitzner, R.; Nazeeruddin, M. K.; Nogueira, A. F.; Odabaşı, Ç.; Osherov, A.; Park, N.-G.; Reese, M. O.; De Rossi, F.; Saliba, M.; Schubert, U. S.; Snaith, H. J.; Stranks, S. D.; Tress, W.; Troshin, P. A.; Turkovic, V.; Veenstra, S.; Visoly-Fisher, I.; Walsh, A.; Watson, T.; Xie, H.; Yildirim, R.; Zakeeruddin, S. M.; Zhu, K.; Lira-Cantu, M. Consensus statement for stability assessment and reporting for perovskite photovoltaics based on ISOS procedures. *Nat. Energy* **2020**, *5* (1), 35–49.
- (8) Jung, E. H.; Jeon, N. J.; Park, E. Y.; Moon, C. S.; Shin, T. J.; Yang, T. Y.; Noh, J. H.; Seo, J. Efficient, stable and scalable perovskite solar cells using poly(3-hexylthiophene). *Nature* **2019**, *567* (7749), 511–515.
- (9) Wang, R.; Xue, J.; Wang, K. L.; Wang, Z. K.; Luo, Y.; Fenning, D.; Xu, G.; Nuryyeva, S.; Huang, T.; Zhao, Y.; Yang, J. L.; Zhu, J.; Wang, M.; Tan, S.; Yavuz, I.; Houk, K. N.; Yang, Y. Constructive molecular configurations for surface-defect passivation of perovskite photovoltaics. *Science* **2019**, *366* (6472), 1509–1513.
- (10) Min, H.; Kim, M.; Lee, S. U.; Kim, H.; Kim, G.; Choi, K.; Lee, J. H.; Seok, S. I. Efficient, stable solar cells by using inherent bandgap of alpha-phase formamidinium lead iodide. *Science* **2019**, *366* (6466), 749–753.
- (11) Kim, G. H.; Jang, H.; Yoon, Y. J.; Jeong, J.; Park, S. Y.; Walker, B.; Jeon, I. Y.; Jo, Y.; Yoon, H.; Kim, M.; Baek, J. B.; Kim, D. S.; Kim,

J. Y. Fluorine Functionalized Graphene Nano Platelets for Highly Stable Inverted Perovskite Solar Cells. *Nano Lett.* **2017**, *17* (10), 6385–6390.

(12) Huang, H.-H.; Ma, Z.; Strzalka, J.; Ren, Y.; Lin, K.-F.; Wang, L.; Zhou, H.; Jiang, Z.; Chen, W. Mild water intake orients crystal formation imparting high tolerance on unencapsulated halide perovskite solar cells. *Cell Reports Physical Science* **2021**, *2* (4), 100395.

(13) Aristidou, N.; Eames, C.; Sanchez-Molina, I.; Bu, X.; Kosco, J.; Islam, M. S.; Haque, S. A. Fast oxygen diffusion and iodide defects mediate oxygen-induced degradation of perovskite solar cells. *Nat. Commun.* **2017**, *8*, 15218.

(14) Song, T.; Feng, X.; Ju, H.; Fang, T.; Zhu, F.; Liu, W.; Huang, W. Enhancing acid, base and UV light resistance of halide perovskite  $\text{CH}_3\text{NH}_3\text{PbBr}_3$  quantum dots by encapsulation with  $\text{ZrO}_2$  sol. *J. Alloys Compd.* **2020**, *816*, 152558.

(15) Chen, P.; Wang, Z.; Wang, S.; Lyu, M.; Hao, M.; Ghasemi, M.; Xiao, M.; Yun, J.-H.; Bai, Y.; Wang, L. Luminescent europium-doped titania for efficiency and UV-stability enhancement of planar perovskite solar cells. *Nano Energy* **2020**, *69*, 104392.

(16) Zhang, Q.; Wang, B.; Zheng, W.; Kong, L.; Wan, Q.; Zhang, C.; Li, Z.; Cao, X.; Liu, M.; Li, L. Ceramic-like stable  $\text{CsPbBr}_3$  nanocrystals encapsulated in silica derived from molecular sieve templates. *Nat. Commun.* **2020**, *11* (1), 31.

(17) Wang, H.; Zhao, Y.; Wang, Z.; Liu, Y.; Zhao, Z.; Xu, G.; Han, T.-H.; Lee, J.-W.; Chen, C.; Bao, D.; Huang, Y.; Duan, Y.; Yang, Y. Hermetic seal for perovskite solar cells: An improved plasma enhanced atomic layer deposition encapsulation. *Nano Energy* **2020**, *69*, 104375.

(18) Shi, L.; Bucknall, M. P.; Young, T. L.; Zhang, M.; Hu, L.; Bing, J.; Lee, D. S.; Kim, J.; Wu, T.; Takamure, N.; McKenzie, D. R.; Huang, S.; Green, M. A.; Ho-Baillie, A. W. Y. Gas chromatography-mass spectrometry analyses of encapsulated stable perovskite solar cells. *Science* **2020**, *368* (6497), No. eaba2412.

(19) Wang, R.; Xue, J. J.; Meng, L.; Lee, J. W.; Zhao, Z. P.; Sun, P. Y.; Cai, L.; Huang, T. Y.; Wang, Z. X.; Wang, Z. K.; Duan, Y.; Yang, J. L.; Tan, S.; Yuan, Y.; Huang, Y.; Yang, Y. Caffeine Improves the Performance and Thermal Stability of Perovskite Solar Cells. *Joule* **2019**, *3* (6), 1464–1477.

(20) Prasanna, R.; Leijtens, T.; Dunfield, S. P.; Raiford, J. A.; Wolf, E. J.; Swifter, S. A.; Werner, J.; Eperon, G. E.; de Paula, C.; Palmstrom, A. F.; Boyd, C. C.; van Hest, M. F. A. M.; Bent, S. F.; Teeter, G.; Berry, J. J.; McGehee, M. D. Design of low bandgap tin-lead halide perovskite solar cells to achieve thermal, atmospheric and operational stability. *Nat. Energy* **2019**, *4* (11), 939–947.

(21) Wang, Y.; Dar, M. I.; Ono, L. K.; Zhang, T.; Kan, M.; Li, Y.; Zhang, L.; Wang, X.; Yang, Y.; Gao, X.; Qi, Y.; Gratzel, M.; Zhao, Y. Thermodynamically stabilized beta- $\text{CsPbI}_3$ -based perovskite solar cells with efficiencies > 18. *Science* **2019**, *365* (6453), 591–595.

(22) Back, H.; Kim, G.; Kim, H.; Nam, C.-Y.; Kim, J.; Kim, Y. R.; Kim, T.; Park, B.; Durrant, J. R.; Lee, K. Highly stable inverted methylammonium lead tri-iodide perovskite solar cells achieved by surface re-crystallization. *Energy Environ. Sci.* **2020**, *13* (3), 840–847.

(23) Huang, H.-H.; Liu, Q.-H.; Tsai, H.; Shrestha, S.; Su, L.-Y.; Chen, P.-T.; Chen, Y.-T.; Yang, T.-A.; Lu, H.; Chuang, C.-H.; Lin, K.-F.; Rwei, S.-P.; Nie, W.; Wang, L. A simple one-step method with wide processing window for high-quality perovskite mini-module fabrication. *Joule* **2021**, *5* (4), 958–974.

(24) Wang, L.; Zhou, H.; Hu, J.; Huang, B.; Sun, M.; Dong, B.; Zheng, G.; Huang, Y.; Chen, Y.; Li, L.; Xu, Z.; Li, N.; Liu, Z.; Chen, Q.; Sun, L. D.; Yan, C. H. A  $\text{Eu}^{3+}$ - $\text{Eu}^{2+}$  ion redox shuttle imparts operational durability to Pb-I perovskite solar cells. *Science* **2019**, *363* (6424), 265–270.

(25) Abdi-Jalebi, M.; Andaji-Garmaroudi, Z.; Cacovich, S.; Stavrakas, C.; Philippe, B.; Richter, J. M.; Alsari, M.; Booker, E. P.; Hutter, E. M.; Pearson, A. J.; Lilliu, S.; Savenije, T. J.; Rensmo, H.; Divitini, G.; Ducati, C.; Friend, R. H.; Stranks, S. D. Maximizing and stabilizing luminescence from halide perovskites with potassium passivation. *Nature* **2018**, *555* (7697), 497–501.

(26) Liu, Z.; Qiu, L.; Ono, L. K.; He, S.; Hu, Z.; Jiang, M.; Tong, G.; Wu, Z.; Jiang, Y.; Son, D.-Y.; Dang, Y.; Kazaoui, S.; Qi, Y. A holistic approach to interface stabilization for efficient perovskite solar modules with over 2,000-h operational stability. *Nat. Energy* **2020**, *5* (8), 596–604.

(27) Sulas-Kern, D. B.; Miller, E. M.; Blackburn, J. L. Photoinduced charge transfer in transition metal dichalcogenide heterojunctions – towards next generation energy technologies. *Energy Environ. Sci.* **2020**, *13* (9), 2684–2740.

(28) Hadadian, M.; Småt, J.-H.; Correa-Baena, J.-P. The role of carbon-based materials in enhancing the stability of perovskite solar cells. *Energy Environ. Sci.* **2020**, *13* (5), 1377–1407.

(29) Jodlowski, A. D.; Roldán-Carmona, C.; Grancini, G.; Salado, M.; Ralaierisoa, M.; Ahmad, S.; Koch, N.; Camacho, L.; de Miguel, G.; Nazeeruddin, M. K. Large guanidinium cation mixed with methylammonium in lead iodide perovskites for 19% efficient solar cells. *Nat. Energy* **2017**, *2* (12), 972–979.

(30) Kim, G. Y.; Senocrate, A.; Yang, T. Y.; Gregori, G.; Gratzel, M.; Maier, J. Large tunable photoeffect on ion conduction in halide perovskites and implications for photodecomposition. *Nat. Mater.* **2018**, *17* (5), 445–449.

(31) Bai, S.; Da, P.; Li, C.; Wang, Z.; Yuan, Z.; Fu, F.; Kawecki, M.; Liu, X.; Sakai, N.; Wang, J. T.; Huettner, S.; Buecheler, S.; Fahlman, M.; Gao, F.; Snaith, H. J. Planar perovskite solar cells with long-term stability using ionic liquid additives. *Nature* **2019**, *571* (7764), 245–250.

(32) Luo, D.; Yang, W.; Wang, Z.; Sadhanala, A.; Hu, Q.; Su, R.; Shivanna, R.; Trindade, G. F.; Watts, J. F.; Xu, Z.; Liu, T.; Chen, K.; Ye, F.; Wu, P.; Zhao, L.; Wu, J.; Tu, Y.; Zhang, Y.; Yang, X.; Zhang, W.; Friend, R. H.; Gong, Q.; Snaith, H. J.; Zhu, R. Enhanced photovoltage for inverted planar heterojunction perovskite solar cells. *Science* **2018**, *360* (6396), 1442–1446.

(33) Wu, S.; Li, Z.; Li, M. Q.; Diao, Y.; Lin, F.; Liu, T.; Zhang, J.; Tieu, P.; Gao, W.; Qi, F.; Pan, X.; Xu, Z.; Zhu, Z.; Jen, A. K. 2D metal-organic framework for stable perovskite solar cells with minimized lead leakage. *Nat. Nanotechnol.* **2020**, *15* (11), 934–940.

(34) Zheng, X.; Chen, B.; Dai, J.; Fang, Y.; Bai, Y.; Lin, Y.; Wei, H.; Zeng, X. C.; Huang, J. Defect passivation in hybrid perovskite solar cells using quaternary ammonium halide anions and cations. *Nat. Energy* **2017**, *2* (7), 17102.

(35) Wang, Z.; McMeekin, D. P.; Sakai, N.; van Reenen, S.; Wojciechowski, K.; Patel, J. B.; Johnston, M. B.; Snaith, H. J. Efficient and Air-Stable Mixed-Cation Lead Mixed-Halide Perovskite Solar Cells with n-Doped Organic Electron Extraction Layers. *Adv. Mater.* **2017**, *29* (5), 1604186.

(36) Brinkmann, K. O.; Zhao, J.; Pourdavoud, N.; Becker, T.; Hu, T.; Olthof, S.; Meerholz, K.; Hoffmann, L.; Gahlmann, T.; Heiderhoff, R.; Oszajka, M. F.; Luechinger, N. A.; Rogalla, D.; Chen, Y.; Cheng, B.; Riedl, T. Suppressed decomposition of organometal halide perovskites by impermeable electron-extraction layers in inverted solar cells. *Nat. Commun.* **2017**, *8*, 13938.

(37) Zhu, Z. L.; Zhao, D. B.; Chueh, C. C.; Shi, X. L.; Li, Z. A.; Jen, A. K. Y. Highly Efficient and Stable Perovskite Solar Cells Enabled by All-Crosslinked Charge-Transporting Layers. *Joule* **2018**, *2* (1), 168–183.

(38) Chen, W.; Wu, Y.; Yue, Y.; Liu, J.; Zhang, W.; Yang, X.; Chen, H.; Bi, E.; Ashraf, I.; Gratzel, M.; Han, L. Efficient and stable large-area perovskite solar cells with inorganic charge extraction layers. *Science* **2015**, *350* (6263), 944–8.

(39) Bai, Y.; Dong, Q.; Shao, Y.; Deng, Y.; Wang, Q.; Shen, L.; Wang, D.; Wei, W.; Huang, J. Enhancing stability and efficiency of perovskite solar cells with crosslinkable silane-functionalized and doped fullerene. *Nat. Commun.* **2016**, *7*, 12806.

(40) Bella, F.; Griffini, G.; Correa-Baena, J. P.; Saracco, G.; Gratzel, M.; Hagfeldt, A.; Turri, S.; Gerbaldi, C. Improving efficiency and stability of perovskite solar cells with photocurable fluoropolymers. *Science* **2016**, *354* (6309), 203–206.

(41) Yang, J.; Liu, C.; Cai, C.; Hu, X.; Huang, Z.; Duan, X.; Meng, X.; Yuan, Z.; Tan, L.; Chen, Y. High-Performance Perovskite Solar

Cells with Excellent Humidity and Thermo-Stability via Fluorinated Peryleneimide. *Adv. Energy Mater.* **2019**, *9* (18), 1900198.

(42) Li, N. X.; Tao, S. X.; Chen, Y. H.; Niu, X. X.; Onwudinanti, C. K.; Hu, C.; Qiu, Z. W.; Xu, Z. Q.; Zheng, G. H. J.; Wang, L. G.; Zhang, Y.; Li, L.; Liu, H. F.; Lun, Y. Z.; Hong, J. W.; Wang, X. Y.; Liu, Y. Q.; Xie, H. P.; Gao, Y. L.; Bai, Y.; Yang, S. H.; Brocks, G.; Chen, Q.; Zhou, H. P. Cation and anion immobilization through chemical bonding enhancement with fluorides for stable halide perovskite solar cells. *Nat. Energy* **2019**, *4* (5), 408–415.

(43) Chang, C. Y.; Huang, H. H.; Tsai, H.; Lin, S. L.; Liu, P. H.; Chen, W.; Hsu, F. C.; Nie, W.; Chen, Y. F.; Wang, L. Facile Fabrication of Self-Assembly Functionalized Polythiophene Hole Transporting Layer for High Performance Perovskite Solar Cells. *Adv. Sci.* **2021**, *8* (5), 2002718.

(44) von Hauff, E.; Dyakonov, V.; Parisi, J. Study of field effect mobility in PCBM films and P3HT:PCBM blends. *Sol. Energy Mater. Sol. Cells* **2005**, *87* (1–4), 149–156.

(45) Nie, W.; Blancon, J. C.; Neukirch, A. J.; Appavoo, K.; Tsai, H.; Chhowalla, M.; Alam, M. A.; Sfeir, M. Y.; Katan, C.; Even, J.; Tretiak, S.; Crochet, J. J.; Gupta, G.; Mohite, A. D. Light-activated photocurrent degradation and self-healing in perovskite solar cells. *Nat. Commun.* **2016**, *7*, 11574.

(46) Juarez-Perez, E. J.; Hawash, Z.; Raga, S. R.; Ono, L. K.; Qi, Y. Thermal degradation of  $\text{CH}_3\text{NH}_3\text{PbI}_3$  perovskite into  $\text{NH}_3$  and  $\text{CH}_3\text{I}$  gases observed by coupled thermogravimetry–mass spectrometry analysis. *Energy Environ. Sci.* **2016**, *9* (11), 3406–3410.

(47) Piersimoni, F.; Degutis, G.; Bertho, S.; Vandewal, K.; Spoltore, D.; Vangerven, T.; Drijkoningen, J.; Van Bael, M. K.; Hardy, A.; D'Haen, J.; Maes, W.; Vanderzande, D.; Nesladek, M.; Manca, J. Influence of fullerene photodimerization on the PCBM crystallization in polymer: Fullerene bulk heterojunctions under thermal stress. *J. Polym. Sci., Part B: Polym. Phys.* **2013**, *51* (16), 1209–1214.

(48) Huang, H. H.; Shih, Y. C.; Wang, L.; Lin, K. F. Boosting the ultra-stable unencapsulated perovskite solar cells by using montmorillonite/ $\text{CH}_3\text{NH}_3\text{PbI}_3$  nanocomposite as photoactive layer. *Energy Environ. Sci.* **2019**, *12* (4), 1265–1273.

(49) Su, L. Y.; Huang, H. H.; Lin, Y. C.; Chen, G. L.; Chen, W. C.; Chen, W.; Wang, L.; Chueh, C. C. Enhancing Long-Term Thermal Stability of Non-Fullerene Organic Solar Cells Using Self-Assembly Amphiphilic Dendritic Block Copolymer Interlayers. *Adv. Funct. Mater.* **2021**, *31*, 2005753.

(50) She, L.; Liu, M.; Zhong, D. Atomic Structures of  $\text{CH}_3\text{NH}_3\text{PbI}_3$  (001) Surfaces. *ACS Nano* **2016**, *10* (1), 1126–31.

(51) Mosconi, E.; Azpiroz, J. M.; De Angelis, F. Ab Initio Molecular Dynamics Simulations of Methylammonium Lead Iodide Perovskite Degradation by Water. *Chem. Mater.* **2015**, *27* (13), 4885–4892.

(52) Zheng, C.; Rubel, O. Unraveling the Water Degradation Mechanism of  $\text{CH}_3\text{NH}_3\text{PbI}_3$ . *J. Phys. Chem. C* **2019**, *123* (32), 19385–19394.

(53) Kakekhani, A.; Katti, R. N.; Rappe, A. M. Water in hybrid perovskites: Bulk  $\text{MAPbI}_3$  degradation via super-hydrous state. *APL Mater.* **2019**, *7* (4), 041112.

(54) Distler, A.; Sauermann, T.; Egelhaaf, H.-J.; Rodman, S.; Waller, D.; Cheon, K.-S.; Lee, M.; Guldi, D. M. The Effect of PCBM Dimerization on the Performance of Bulk Heterojunction Solar Cells. *Adv. Energy Mater.* **2014**, *4* (1), 1300693.

(55) Kim, T.; Younts, R.; Lee, W.; Lee, S.; Gundogdu, K.; Kim, B. J. Impact of the photo-induced degradation of electron acceptors on the photophysics, charge transport and device performance of all-polymer and fullerene–polymer solar cells. *J. Mater. Chem. A* **2017**, *5* (42), 22170–22179.

(56) Heumueller, T.; Mateker, W. R.; Distler, A.; Fritze, U. F.; Cheacharoen, R.; Nguyen, W. H.; Biele, M.; Salvador, M.; von Delius, M.; Egelhaaf, H.-J.; McGehee, M. D.; Brabec, C. J. Morphological and electrical control of fullerene dimerization determines organic photovoltaic stability. *Energy Environ. Sci.* **2016**, *9* (1), 247–256.

(57) Ball, J. M.; Petrozza, A. Defects in perovskite-halides and their effects in solar cells. *Nat. Energy* **2016**, *1* (11), 16149.

(58) Sherkar, T. S.; Momblona, C.; Gil-Escrig, L.; Avila, J.; Sessolo, M.; Bolink, H. J.; Koster, L. J. A. Recombination in Perovskite Solar Cells: Significance of Grain Boundaries, Interface Traps, and Defect Ions. *ACS Energy Lett.* **2017**, *2* (5), 1214–1222.

(59) Han, Y.; Meyer, S.; Dkhissi, Y.; Weber, K.; Pringle, J. M.; Bach, U.; Spiccia, L.; Cheng, Y. B. Degradation observations of encapsulated planar  $\text{CH}_3\text{NH}_3\text{PbI}_3$  perovskite solar cells at high temperatures and humidity. *J. Mater. Chem. A* **2015**, *3* (15), 8139–8147.

(60) Boyd, C. C.; Cheacharoen, R.; Leijtens, T.; McGehee, M. D. Understanding Degradation Mechanisms and Improving Stability of Perovskite Photovoltaics. *Chem. Rev.* **2019**, *119* (5), 3418–3451.

(61) Montcada, N. F.; Mendez, M.; Cho, K. T.; Nazeeruddin, M. K.; Palomares, E. Photo-induced dynamic processes in perovskite solar cells: the influence of perovskite composition in the charge extraction and the carrier recombination. *Nanoscale* **2018**, *10* (13), 6155–6158.

(62) Zhang, H.; Fu, X.; Tang, Y.; Wang, H.; Zhang, C.; Yu, W. W.; Wang, X.; Zhang, Y.; Xiao, M. Phase segregation due to ion migration in all-inorganic mixed-halide perovskite nanocrystals. *Nat. Commun.* **2019**, *10* (1), 1088.

(63) Fang, H. H.; Yang, J.; Tao, S. X.; Adjokatse, S.; Kamminga, M. E.; Ye, J. T.; Blake, G. R.; Even, J.; Loi, M. A. Unravelling Light-Induced Degradation of Layered Perovskite Crystals and Design of Efficient Encapsulation for Improved Photostability. *Adv. Funct. Mater.* **2018**, *28* (21), 1800305.